PANS and DES of a Simplified Heavy-Duty Vehicle. Comparison and an Active Flow Control Application

Miguel Calixto de Sousa
miguel.calixto.sousa@tecnico.ulisboa.pt

Instituto Superior Técnico, Universidade de Lisboa, Portugal
November 2018

***Abstract*—This work presents two main purposes: one is to see how the partially-averaged Navier-stokes (PANS) method performs against the detached eddy simulation (DES) method for different grid refinement levels, when applied to the study of the external aerodynamics of a generic heavy-duty vehicle, and the other is to study the application of Active Flow Control (AFC) on the trailer front pillars of a generic heavy-duty vehicle, on a dynamic oscillating configuration, using PANS.**

For the first part, a cross analysis of the flow physics around the generic heavy-duty vehicle and a comparison of the time-averaged and the instantaneous flow structures, force coefficients and aerodynamic forces of the results obtained using DES and PANS with three grids of different level of refinement, is performed. The results show that both PANS and DES simulations capture the same main flow features and produce similar trends, which are in accordance with published works. The DES shows more robustness, as its results using the three different meshes are more similar than in PANS, and it handles the coarser mesh better, since the PANS results with the coarse mesh show a significant deviation from the ones using the more refined meshes.

For the second part, the heavy-duty model is simulated to have a dynamic oscillation of the yaw angle between $-10^\circ < \beta < 10^\circ$ with a non-dimensional frequency $St = fW/U_{inf} = 0.1$, with and without the actuation of AFC in the trailer front pillars. Overall, the actuation is not effective and even shows to be disadvantageous.

I. Introduction

The need of reducing fuel consumption and greenhouse gas (GHG) emissions gets more important day by day. Since the aerodynamic drag accounts for more than 60% of the total power consumption of a traveling truck at cruising speed, [1], the improvement of its aerodynamic efficiency is imperative for the reduction of the total power consumption. For that, a good understanding of its aerodynamics is fundamental, and a very famous tool for predicting the flow around an heavy-duty vehicle is Computational Fluid Dynamics (CFD). The flow around an Heavy-duty vehicle is characterized by large separation regions, where unsteadiness governs the flow. Different approaches to solve the flow field are available and the choice between methods is a compromise between flow resolution and computational resources available. The Reynolds Averaged Navier-Stokes (RANS) model does not require a fine grid, however it fails to describe massively separated flows, as it cannot predict wake and vortex flows, due to the inadequate modeling of the turbulence. Direct numerical simulation (DNS) requires very fine spatial and temporal resolution, in order to resolve the whole spectrum of spatial and temporal scales of turbulence, which makes it prohibitive for industrial turbulent flows. The large-eddy simulation (LES) method decreases the computational cost, when compared to DNS, by modelling the small length scales, which are the most computationally expensive to resolve, only resolving the larger scales, however, it still is too resource expensive.

The inaccuracy of the steady RANS and the expensiveness of the DNS and LES techniques have led to pursue the hybridization and bridging between the RANS modeling approaches and the flow resolving approaches, LES and DNS. The detached-eddy simulation (DES) is the most popular hybrid method in the research community and industry, as it has been successful in predicting the flow around bluff bodies, like trains [2], and Ahmed bodies [3]. The base of DES is that it behaves as LES in the regions away from the near-wall where there is a large separation of the flow and fine enough resolution, and as unsteady RANS (URANS) models everywhere else. The partially-averaged Navier–Stokes (PANS) is based in the bridging between RANS and DNS depending on the dynamic control parameters f_k and f_ϵ, which are dependent on the flow local characteristics and local grid dimensions. This way, the PANS model will behave as RANS on regions of low turbulence and coarser grid and as DNS in regions of high turbulence and refined enough mesh. The PANS method has been successful in solving the flow around different bluff bodies, like landing gears, [4], and a generic truck cabin with AFC application, [5].

In the first part of the present work, static PANS and DES simulations of the flow around a truck model, at a Reynolds number $\mathrm{Re} = 2.5 \times 10^5$, (based on the width of the model, $W = 0.4$ m), have been performed. For each method, three equivalent simulations are ran using a common coarse (3 million cells) , medium (5 million cells) and fine mesh (8 million cells). The use of this resolutions

in PANS cases of similar geometries, domain, conditions and with the same characteristic length, W, have previously been validated in the study of the application of AFC on a generic truck cabin, [5], and the application of AFC on a oscillating truck cabin, [6]. The objective of this simulations is not only to understand the model flow nature, but also to compare the capability of PANS and DES in predicting the unsteady turbulent flow around the model, how they behave with refinement of the mesh and how they compare with PIV experimental results in the wake of the trailer.

After the first part, the focus changes from understanding the flow in static condition and how the PANS and DES models compare to each other, to work on the improvement of the vehicle's efficiency, specifically, through Active Flow Control (AFC) application. The goal of applying AFC on a heavy-duty vehicle is to mitigate the large scale flow separation, which usually occurs at the gap between the tractor and the trailer, at the wheel-housing and wheels, the under-body and majorly the trailer wake region, [7]. There are several AFC techniques, and the one used in this work is the zero net mass flux (ZNMF) synthetic jet with a constant frequency, where air is sucked in and pumped by the oscillation of a membrane. This control technique have been extensively used in different aerodynamic fields to mitigate flow separation. Inclusive, it was implemented to manipulate the wake of generic vehicles, [8], control the flow separation at the A-pillar of oscillating simplified truck cabins, [6], and truck-trailer models, [7].

Based on the major success of the AFC application in the truck cabin presented in previous works mentioned, one of the current work aims is to present a solution to the drag induced in the gap region by application of AFC, in close to real conditions, where the presence of front and side wind gusts lead to a large separation of the flow in the trailer front pillars, extending along the side surfaces of it. The use of AFC on the front pillars of the trailer is not only very advantageous for heavy-duty vehicles without the possibility to have cab extenders, but it could also be for the ones that do, as it may perform better under realistic conditions, under which the cab extenders work poorly, [9]. Also, with the use of AFC, the radius of the trailer front pillars can be decreased, increasing this way the space inside the trailer while having a good aerodynamic performance.

So, the second part focus is on starting to access how viable is the application of the active flow control (AFC) technique zero net mass flux (ZNMF) pulsating synthetic jet in the trailer front pillars, in order to mitigate the flow separation and consequently enhancing its aerodynamic performance on the gap region during close to real conditions. Here, two simulations of an oscillating simplified truck model are carried out, one with the application of AFC in the front trailer pillars and one without. In this simulations the PANS method is used, and the model studied is the same as in the first part of this thesis, but with a wider trailer of $W = 0.45$ m. The studies are made using geometry and meshes similar to the ones the ones used in the first part of the project, which are based in already validated cases in [5] and [6], which also validate the application of PANS in AVL-Fire, under the same conditions, through experiments.

II. Modelling turbulence

A. The PANS equations

The PANS model implemented in this thesis is the PANS $\zeta - f$, through the commercial code AVL Fire. The Incompressible Navier-Stokes equation for the instantaneous velocity (V) and pressure (p) fields is:

$$\frac{\partial V_i}{\partial t} + V_j \frac{\partial V_i}{\partial x_j} = -\frac{\partial p}{\partial x_i} + \nu \frac{\partial^2 V_i}{\partial x_j \partial x_j}. \tag{1}$$

The PANS model takes the decomposition, $V_i = U_i + u_i; p = p_U + p_u$. The unresolved velocity, u_i, and unresolved pressure, p_u, are of background turbulence and are modeled, while $U_i =< V_i >$; $p_U =< p >$ are the partially-averaged (filtered) flow variables, and are resolved, where $<>$ denotes an arbitrary filter which is commutative with the spatial and temporal differentiation. This way, the PANS equation is written as:

$$\frac{\partial U_i}{\partial t} + U_j \frac{\partial U_i}{\partial x_j} = -\frac{\partial p_U}{\partial x_i} + \frac{\partial}{\partial x_j}\left(\nu \frac{\partial U_i}{\partial x_j} + \tau(V_i, V_j)\right), \tag{2}$$

where $\tau(V_i, V_j) =< V_i V_j > - < V_i >< V_j >$ is the subfilter scale (SFS) stress, which represents the effect of the unresolved scales on the resolved field, and it is closed by its anisotropic part using the eddy-viscosity (Boussinesq) assumption, $\tau(V_i, V_j) = -2\nu_u S_{ij} + \frac{2}{3} k_u \delta_{ij}$, where k_u is the unresolved (subfilter) turbulent kinetic energy, $S_{ij} = \frac{1}{2}\left(\frac{\partial U_i}{\partial x_j} + \frac{\partial U_i}{\partial x_i}\right)$ is the resolved stress tensor, and $\nu_u = C_\mu \zeta_u \frac{k_u^2}{\epsilon_u}$ is the viscosity of the unresolved scales.

In order to close the model, three transport equations for $k - \epsilon - \zeta$ and a Poisson equation, for the elliptic relaxation function of the unresolved velocity scales, f_u, are necessary. So, the PANS $\zeta - f$ model is constituted by the set of equations:

$$\begin{aligned}
\frac{\partial k_u}{\partial t} + U_j \frac{\partial k_u}{\partial x_j} &= P_u - \epsilon_u + \frac{\partial}{\partial x_j}\left(\frac{\nu_u}{\sigma_{k_u}} \frac{\partial k_u}{\partial x_j}\right) \\
\frac{\partial \epsilon_u}{\partial t} + U_j \frac{\partial \epsilon_u}{\partial x_j} &= C_{\epsilon 1} P_u \frac{\epsilon_u}{k_u} - C^*_{\epsilon 2} \frac{\epsilon_u^2}{k_u} + \frac{\partial}{\partial x_j}\left(\frac{\nu_u}{\sigma_{\epsilon_u}} \frac{\partial \epsilon_u}{j}\right) \\
C^*_{\epsilon 2} = C_{\epsilon 1} + f_k(C_{\epsilon 2} - C_{\epsilon 1}); \qquad & C_{\epsilon 1} = 1.4\left(1 + \frac{0.045}{\sqrt{\zeta_u}}\right) \\
\frac{\partial \zeta_u}{\partial t} + U_j \frac{\partial \zeta_u}{\partial x_j} &= f_u - P_u \frac{\zeta_u}{k_u} + \frac{\zeta_u}{k_u} \epsilon_u (1 - f_k) + \\
&\quad + \frac{\partial}{\partial x_j}\left(\frac{\nu_u}{\sigma_{\zeta_u}} \frac{\partial \zeta_u}{\partial x_j}\right) \\
L_u^2 \nabla^2 f_u - f_u &= \frac{1}{T_u}\left(c_1 + c_2 \frac{P_u}{\epsilon_u}\right)\left(\zeta_u - \frac{2}{3}\right),
\end{aligned} \tag{3}$$

where $P_u = -\tau(V_i, V_j)\frac{\partial U_i}{\partial x_j}$ is the production of unresolved turbulent kinetic energy, which is closed by the previously introduced Bousinnesq assumption. The constants in Eqs. 3 are $C_\mu = 0.22$, $C_{\epsilon 2} = 1.9$, $c_1 = 0.4$, $c_2 = 0.65$, $\sigma_k = 1$, $\sigma_\epsilon = 1.3$, $\sigma_u = 1.2$. L_u and T_u are the length and time scales, respectively, and are defined as, $T_u = \max\left[\frac{k_u}{\epsilon}, C_\tau\left(\frac{\nu}{\epsilon}\right)^{1/2}\right]$, $L_u = C_L \max\left[\frac{k^{3/2}}{\epsilon}, C_\eta\left(\frac{\nu^3}{\epsilon}\right)^{1/4}\right]$, where $C_\tau = 6$, $C_L = 0.36$, $C_\eta = 85$.

The parameters $f_{k,\epsilon}$ dynamically determine how much of the flow is resolved, as they vary between 0 and 1. In the PANS $\zeta - f$ set of equations, it was assumed that $f_\epsilon = \frac{\epsilon_u}{\epsilon} = 1$, which means that all the unresolved dissipation is assumed to be RANS dissipation and therefore modeled. This assumption is based on the fact that in most cases the small dissipative scales are unlikely to be resolved, since a computational grid beyond the inertial subrange, i.e. a near wall DNS resolution, would be required. Leaving only the crucial variable f_k to be chosen. When f_k assumes the value of one it makes the set of PANS $\zeta - f$ equations turn into the base RANS equations, assuming the value of zero makes it turn into the DNS approach, and assuming values in between makes it behave as mixture of RANS and DNS. As the influence of f_k on the resolved flow physics became clearer over time, its value evolved from being a fixed value to a dynamic parameter, where at every time-step the smallest value of f_k that a grid can support is calculated for every computational cell. In order to fulfill this, the following dynamic parameter was proposed:

$$f_k(x,t) = \frac{1}{C_\mu}\left(\frac{\Delta}{\Lambda}\right)^{2/3}, \tag{4}$$

where Δ is the geometric-average grid cell dimension, $\Delta = (\Delta x \cdot \Delta y \cdot \Delta z)^{1/3}$, and Λ is the Tayler scale of turbulence, which is computed as $\Lambda = \frac{(k_u + k_{res})^{1.5}}{\epsilon}$, where k_{res} is the resolved kinetic energy.

B. The DES equations

The variant of DES used in this project is the SST (Menter) $k-\omega$ Detached Eddy simulation, with an Improved Delayed DES (IDDES) formulation, through the STAR-CCM+ commercial code. An overview of the formulation of this model is now presented.

The base model in which it is set is the SST $k-\omega$ model, in which the transport equations for the kinetic energy, k, and the specific dissipation rate, ω, are:

$$\frac{\partial}{\partial t}(\rho k) + \nabla\cdot(\rho k\overline{u}) = \nabla\cdot[(\mu + \sigma_k\mu_t)\nabla k] + P_k - \rho\beta^* f_{\beta^*}(\omega k - \omega_0 k_0) + S_k \tag{5}$$

$$\begin{aligned}\frac{\partial}{\partial t}(\rho\omega) + \nabla\cdot(\rho\omega\overline{u}) = \nabla\cdot[(\mu + \sigma_\omega\mu_t)\nabla\omega] + P_\omega - \rho\beta(\omega^2 - \omega_0^2 k_0) + \\ + 2\rho(1-F_1)\sigma_{w_2}\frac{1}{\omega}\nabla k\cdot\nabla\omega + S_\sigma,\end{aligned} \tag{6}$$

where $\overline{u}$ is the mean velocity, μ is the dynamic viscosity, k_0 and ω_0 are the ambient turbulence values that counteract turbulence decay, and S_k and S_ω are the user-specified source terms. f^*_β is the free-shear modification factor, which is a dissipation limiter that counteracts the $k-\omega$ model tendency to underpredict the production of ω in flows that are dominated by free-shear layers (such as jets or mixing layers) or when free-stream turbulence is high. The P_k and P_ω are production terms, where $P_k = G_k + G_{nl}$, G_k being the turbulent production, and G_{nl} the "non-linear" production: $P_\omega = \rho\gamma\left[\left(S^2 - \frac{2}{3}(\nabla\cdot\overline{u})^2\right) - \frac{2}{3}\omega\nabla\cdot\overline{u}\right]$, $G_k = \mu_t f_c S^2 - \frac{2}{3}\rho k\nabla\cdot\overline{u} - \frac{2}{3}\mu_t(\nabla\cdot\overline{u})^2$, $G_{nl} = \nabla\cdot\overline{u} : (T_{t,NL})$, where the : represents a inner product of two tensors, γ is a model coefficient defined later in this section, f_c is the curvature correction factor, which incorporates the stabilizing and destabilizing effects usually associated with strong (streamline) curvature and frame rotation (to which the transport equation for the turbulent kinetic energy is insensitive, by construction), [10], $S = \sqrt{2S_{ij}S_{ij}}$ is the modulus of the mean strain rate tensor (with $S_{ij} = \frac{1}{2}\left(\frac{\partial\overline{u}_i}{\partial x_j} + \frac{\partial\overline{u}_j}{\partial x_i}\right)$ being the mean strain rate tensor), and $T_{t,NL}$ is a quadratic non-linear constitutive relation, which accounts for anisotropy of turbulence by adding non-linear functions of the strain and vorticity tensors. The third term of the right end side of Eq. 6 is the cross diffusion term, which makes the $k-\omega$ model behave like the $k-\epsilon$ model, and its influence on the model is controlled by F_1, the blending function responsible for changing the behaviour of the SST model between the $k-\omega$ and $k-\epsilon$ formulation by changing between the value 1 close to the wall, to 0 in the outer part of the boundary layer and outside of it, and is defined as $F_1 = \tanh\left(\left[\min\left(\max\left(\frac{\sqrt{k}}{0.09\omega d}, \frac{500\nu}{d^2\omega}\right), \frac{2k}{d^2 CD_{k\omega}}\right)\right]^4\right)$, where $CD_{k\omega} = \max(\frac{1}{\omega}\nabla k\cdot\nabla\omega, 10^{-20})$ is the cross-diffusion coefficient. In the transport equations, Eq. 5 and 6, there are also present some model coefficients, σ_k, β^*,σ_ω, β and γ, which are calculated as:

$\sigma_k = F_1\sigma_{k_1} + (1-F_1)\sigma_{k_2}$	$\sigma_{k_1} = 0.85$;	$\sigma_{k_2} = 1$
$\beta^* = F_1\beta^*_1 + (1-F_1)\beta^*_2$	$\beta^*_1 = 0.09$;	$\beta^*_2 = 0.09$
$\sigma_\omega = F_1\sigma_{\omega_1} + (1-F_1)\sigma_{\omega_2}$	$\sigma_{\omega_1} = 0.5$;	$\sigma_{\omega_2} = 0.856$
$\beta = F_1\beta_1 + (1-F_1)\beta_2$	$\beta_1 = 0.075$;	$\beta_2 = 0.0828$
$\gamma = F_1\gamma_1 + (1-F_1)\gamma_2$	$\gamma_1 = \frac{\beta_1}{\beta^*} - \sigma_{\omega_1}\frac{k^2}{\sqrt{\beta^*}}$	$\gamma_2 = \frac{\beta_2}{\beta^*} - \sigma_{\omega_2}\frac{k^2}{\sqrt{\beta^*}}$

The SST $k-\omega$ model is equipped with a turbulent shear stress limiter which switches from a eddy viscosity model to the Johnson-King (JK) model for most of the adverse pressure gradient regions (wake region of the boundary layer), i.e. where the shear stress becomes excessively large, [11] and [12]. The turbulent viscosity is defined as $\mu_t = \rho k T$, where $T = \min\left(\frac{1}{\omega}, \frac{a_1}{SF_2}\right)$ is the turbulent time scale, which is calculated using Durbin's realizability constraint. $a_1 = 0.31$ is a model coefficient and $F_2 = \tanh\left(\left(\max\left(\frac{2\sqrt{k}}{\beta^*\omega d}, \frac{500\nu}{d^2\omega}\right)\right)^2\right)$ is a blending function that ensures that the JK model can only be used in the boundary layer, where d is is the distance to the wall.

The used DES formulation of the (Menter) SST $k-\omega$ model, using the IDDES approach, is based on the work of Shur et al., [13], and is obtained by replacing the specific dissipation rate, ω, in the transport equation for

the turbulent kinetic energy, Eq. 5, of the RANS SST $k-\omega$ model, by $\tilde{\omega} = \frac{\sqrt{k}}{l_{\text{HYBRID}}\beta^* f_{\beta^*}}$, where l_{HYBRID} is the variable containing the filter that makes the model switch between the RANS and LES mode:

$$l_{\text{HYBRID}} = \tilde{f}_d(1+f_e)l_t + (1-\tilde{f}_d)C_{\text{DES}}\Delta_{\text{IDDES}}, \quad (7)$$

where l_t is the RANS length scale, which for the (Menter) SST $k-\omega$ is calculated as $l_t = k^{1/2}/(\beta^*\omega)$, which makes the RANS-LES switch dependent on the flow and not only on the grid, since it depends on k and ω. $C_{\text{DES}}\Delta_{\text{IDDES}}$ is the LES length scale, where $\Delta_{\text{IDDES}} = \min(\max(0.15d, 0.15\Delta, \Delta_{\min}), \Delta))$ is the altered SGS filter of LES used, where d is the distance to the wall, Δ is the largest distance between the cell center under consideration and the cell centers of the neighboring cells and $\Delta_{\min}$ is the smallest distance between the cell center under consideration and the cell centers of the neighboring cells. Unlike the usual LES and DES approaches, this new definition of the subgrid length-scale includes explicit wall-distance dependence, and not only the grid-spacings. As previously stated, the IDDES approach is constituted by two branches, one that is the WMLES mode, which is only activated when the inflow conditions used in the simulation are unsteady and impose some turbulent content and the grid is fine enough to resolve boundary-layer dominant eddies, and other which is the DDES mode. The WMLES branch is introduced to the length scale calculation, Eq. 7, by the blending function f_B and the so-called "elevating" function, f_e. The function $f_B = \min\left[2\exp(-9\alpha^2), 1\right]$ is only dependent on the grid construction, where $\alpha = 0.25 - \frac{d}{\Delta}$, which it varies from 0 to 1, while providing rapid switching of the model from RANS mode ($f_B = 1$) to LES mode ($f_B = 0$) within the range of wall-distance $0.5\Delta < d < \Delta$. f_e has the aim of preventing the excessive reduction of the RANS Reynolds stresses, observed in the interaction of the RANS and LES regions, in the vicinity of their interface, combating this way the log-layer mismatch. f_e is defined in a way that it is close to zero (passive) in two occasions:

- when the grid used is sufficient for a wall-resolved LES (the interface between RANS and LES occurs very close to the wall, $y^+ < 15 \sim 20$, making the Reynolds stresses near the interface negligible);
- when the model performs as the background RANS model.

Such requirements are met by using the definition $f_e = \max[(f_{e_1} - 1), 0]\psi f_{e_2}$, where the introduction of the function ψ is purely empirical and f_e is only active in the RANS simulation region, i.e. where $f_B = 1$. f_{e_1} is the shape function of f_e , while the amplitude of f_e depends on the solution field, and is given by f_{e_2}. This component is built of sensor functions for the viscous sublayer and for the modeled log-law region, r_{dl} and r_dt respectively.

$$f_{e_1} = \begin{cases} 2\exp(-11.09\alpha^2), & \text{if } \alpha \geq 0 \\ 2\exp(-9\alpha^2), & \text{if } \alpha \leq 0 \end{cases}$$

$f_{e_2} = 1 - \max(f_t, f_l)$ controls the intensity of "elevating" of the RANS component of the model through the functions:

$$f_t = \tanh[(C_t^2 r_{dt})^3]; \quad C_t = 1.87; \quad r_{dt} = \frac{\nu_t}{\sqrt{\nabla u : \nabla u^T} k^2 d^2}$$

$$f_l = \tanh[(C_l^2 r_{dl})^1 0]; \quad C_l = 5; \quad r_{dl} = \frac{\nu}{\sqrt{\nabla u : \nabla u^T} k^2 d^2}$$

where $k = 0.41$ is the Von Karman constant. C_l and C_t are specific constants from the model, which are tuned so that f_{e_2} is virtually zero when either f_t or f_l are close to unity. The function $\tilde{f}_d$ is the blending function that combines the WMLES and DDES branches of the model and is defined as $\tilde{f}_d = \max((1-f_{dt}), f_B)$, with $f_{dt} = 1 - \tanh\left[(C_{dt} r_{dt})^3\right]$, where $C_{dt} = 20$ is a mode coefficient.

III. Numerical set-up

All simulations use a time step of $\Delta t = 5\text{x}10^{-5}$ s, which gives a CFL number, $CFL = \frac{U_\infty \Delta t}{\Delta x}$, lower than 1, in all the domain, providing this way a good time accuracy. The static simulations were all set at $\text{Re} = 2.5 \times 10^5$, based on the inlet velocity $U_\infty = 9.438$ m/s, and the width of the model, $W = 0.4$ m. All dimensions are on Fig. 1 and 2.

For all static simulations, the following boundary conditions were applied: an inlet condition at the entrance of the domain with a constant, normal to the surface velocity of $U_\infty = 9.438$ m/s; a symmetry condition for both side walls and the roof of the channel; an homogeneous Neumann boundary condition, $gradient = 0$; no-slip condition boundary condition was applied to all the surfaces of the truck model as well as to the floor.

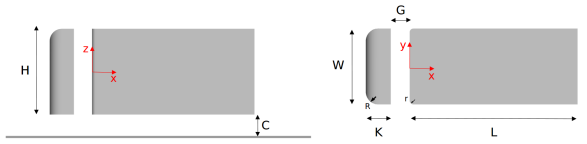

a) b)

Figure 1: The model geometry.

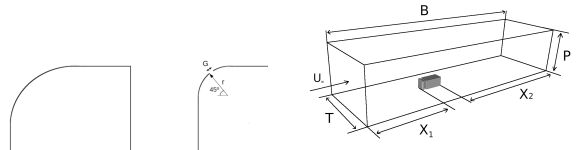

a) b)

Figure 2: Representation of the top view of the AFC slot, a), and of the domain, b).

H/W	c/W	K/W	G/W	L/W	T/W	P	B
1.1675	0.167	0.33	0.25	2.22	9	6.25	29.65

Table I: Dimensions of the model and domain.

The details of three computational grids are reported on table II.

Case	Coarse mesh	Medium mesh	Fine mesh
Cells (M)	3	5.1	7.9
y^+_{max}	3.7	3.1	2.9
y^+_{mean}	0.344	0.346	0.341
$\Delta^+_{s\,max}$	630	465	374
$\Delta^+_{l\,max}$	358	286	240

Table II: Details of the computational grids. Number of cells in millions.

A. Creating the Dynamic Case

For the dynamic simulations the width of the trailer was changed to $W = 0.45$ m, in order to give a bigger separation at the trailer front pillar, setting this way a model where the application of AFC can be more beneficial. The mesh used was derived from the medium refinement mesh of the static simulations. Two dynamic simulations were conducted, one with AFC application and one without. The simulation of the dynamic truck oscillation in the yaw direction between the two extreme angles was implemented by changing the inlet, roof and side walls boundary conditions to an inlet boundary condition with a specified u and v velocity varying in time. To define the oscillation formula for the boundaries, two main parameters that describe this oscillation have to be set. The first one is the oscillation frequency, which is set to have a Strouhal frequency of $\mathrm{St} = \frac{fW}{U_\infty} = 0.1$, where f is the oscillation frequency in Hz, W is the trailer width and $U_\infty = 9.438$ m/s is the module of the inlet velocity. The second one is the range of the yaw angle, $-10° < \beta < 10°$. These choices are supported by experiments performed in real conditions [14, 15, 16], which give $0.06 < \mathrm{St} < 0.9$ as important frequencies in crosswind studies, and a lateral wind speed of around 4-5 m/s, [14], which leads to the chosen yaw angle range. These parameter were also chosen to match the ones in [6], which studies the application of AFC in the A-pillars of an oscillating truck cabin, where the model has a similar geometry and the same AFC actuation reduced frequency. The dynamic oscillation is then described by a sinusoidal oscillation which is given by the formulas:

$$\begin{cases} u = 9.366 + 0.0717\cos(8.4\pi(t - t_0)), \\ v = 1.6389\sin(4.2\pi(t - t_0)), \end{cases} \tag{8}$$

where u and v are the streamwise and spanwise velocities set on the boundaries, t is the time and t_0 is the time the oscillation started in the simulation. For both dynamic simulations, around 0.5 s (half a passage) were ran with the static settings, after which the dynamic conditions were implemented. The results started being averaged after one full sweeping cycle and were ran for two more cycles.

B. AFC application

In an attempt to decrease the separation on the front pillars of the trailer, AFC is applied in the dynamic configuration. The AFC applied is a zero net mass flux pulsating synthetic jet, applied through a 1.01 mm slot, in the direction normal to the surface, as represented in Fig. 2. a). The suction and blowing of the synthetic jet actuator is simulated through an inlet boundary condition with a time varying velocity normal to the surface given by the sinusoidal equation

$$U_{AFC} = 0.26U_\infty \sin(t2\pi f_a), \tag{9}$$

where f_a is the actuation frequency. f_a is chosen based on [6], where the application of the same type of AFC with a reduced frequency of $F^+ = \frac{f_a}{U_{inf}/W} = 3.1$ is applied in the A-pillars of an oscillating truck cabin, with a successfully omission of separation on the A-pillar and resulting in a considerable C_d reduction. The use of the same reduced frequency, with a $W = 0.45$ m leads to an actuation frequency of $f_a = 65Hz$.

C. Solver parameters

In this work PANS and DES were used as the solving methods for the numerical simulations. The static simulations were solved using both PANS and DES while the dynamic simulations were solved using only PANS. The PANS method was applied using the commercial finite-volume based CFD software AVL-Fire, and the DES method using STAR-CCM+.

For both methods, a hybrid wall-treatment was chosen and the time marching procedure was done using the implicit second order accurate three time level scheme. In PANS simulations, the continuity equation have been discretized with central differencing scheme (CDS), the turbulence equations with a second order upwind scheme MINMOD to approximate the convective fluxed, [17], and the momentum equation with AVL SMART Bounded, [18]. Under-relaxation factor parameters were introduced in order to guarantee the stability of the equations. A maximum of eight iterations for each time-step was imposed.

For the DES simulations, a segregated solver with Hybrid Second-Order Upwind/Bounded-Central discretization scheme is used.

IV. Static results

A. Drag Coefficient, C_d

Grid	Cabin	Trailer	Truck
Coarse DES	0.7121	-0.2321	0.4800
Medium DES	0.707838	-0.2329	0.4749
Fine DES	0.6876	-0.2096	0.4780
Coarse PANS	0.7020	-0.2436	0.4585
Medium PANS	0.7039	-0.2390	0.4648
Fine PANS	0.6706	-0.2143	0.4564

Table III: Mean values of C_d.

The mean values of the drag coefficient can be seen in Table III. By comparing the mean value of the full truck's C_d between meshes, the coarse has a difference of less than 0.5% when compared to the fine mesh for both PANS and DES models, and the difference between the methods for each mesh is always below 5%. Showing a very close degree of accuracy in predicting C_d between the different meshes

and between methods. One can see that the C_d values for the cabin and trailer are also considerably close across methods and meshes.

By proving both methods give similar predictions of C_d across the meshes, this section also serves as a mesh independence study.

B. Lift Coefficient, C_l

The lift coefficient is also of great importance since it is directly connected with vehicles traction, stability and overall dynamic performance.

Grid	Cabin	Trailor	Truck
Coarse DES	0.1728	-0.3206	-0.1477
Medium DES	0.1773	-0.3244	-0.1471
Fine DES	0.1766	-0.3293	-0.1527
Coarse PANS	0.1327	-0.2822	-0.1495
Medium PANS	0.1905	-0.3198	-0.1293
Fine PANS	0.1923	-0.3321	-0.1398

Table IV: Mean values of C_l.

The Table IV presents the mean values of lift coefficient. For the full truck, the mean value of C_l obtained with the coarse mesh has a difference of around 3.3% when compared to the fine mesh for DES models, which is very close. For the PANS the difference is of around 6.9%. However, for PANS, when comparing the medium mesh truck's C_l with the fine mesh, we get a difference of 15.6% which is considerably higher but still acceptable. Still for PANS, the difference between coarse and fine mesh is -31% and -15% for the cabin and trailer respectively, and -0.88% and -3.7% between medium an fine mesh for the cabin and trailer respectively. All in all, we can say that the C_l values are considerably closer between meshes for the DES than for PANS.

C. Velocity and Reynolds stress profiles on the wake

In this section, the velocity and Reynolds stress profiles, taken on the plane $z = 0$ along $x^* = x/W = 3.0304$, are analyzed for three levels of grid refinement, and are compared with the experimental results obtained through PIV in an equivalent to the numerical simulation settings. The value of mean velocity in the x and y direction and the mean Reynolds stresses $\overline{u'u'}$ and $\overline{v'v'}$ were recorded after 5 passages for each method and mesh, and are presented in Fig. 3 and 4, respectively.

Looking at Fig. 3, one can see that the u/U_{inf} profiles obtained from the numerical simulations always over-predicts the magnitude when compared to the PIV results. All results show a conical profile, symmetric or close to symmetric in relation to $y = 0$.

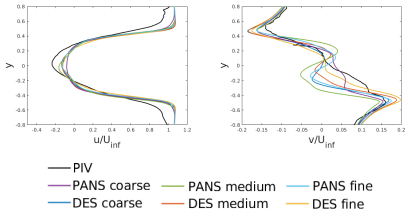

Figure 3: Profiles of the time-averaged velocity in the stream-wise and span direction at $x^* = 3.0304$, on the $z^* = 0$ plane.

The profiles obtained with the simulations show a very good agreement between both methods across the three meshes, as they overlap along big portions of the profiles, showing again a good mesh convergence. One can again see that the coarse mesh results are further apart from the medium and fine mesh. The biggest differences between the CFD and experimental results are in the region closer to the interior of the profile. Again, the DES results present better agreement between meshes than the PANS results, and the PANS with the coarse mesh is the case which present most different profiles. All numerical simulations are similarly distant from the PIV results.

Now looking at v/U_{inf}, the profiles of velocity in the span-wise direction, one can see that the simulation results give significantly different results, when compared to the PIV ones, specially when closer to the core region of the wake, $y = 0$.

Overall, both methods, across all meshes, don't capture the peaks of u and v velocity precisely, but all capture the trends present in PIV results.

The differences in the profiles between the simulations and the PIV results described this section, until now, can be justified by differences between the simplified truck models used in the simulations and in the experiments, specially from the existence of two connecting rods between the cabin and trailer and of the round support located underneath the trailer, which have a major influence on the flow underneath the model that strongly propagates to the wake.

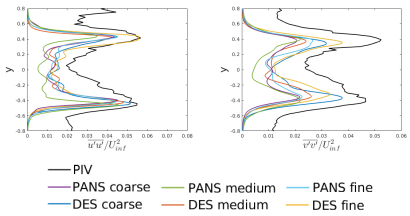

Figure 4: Profiles of $\frac{\overline{u'u'}}{U_{inf}^2}$ and $\frac{\overline{v'v'}}{U_{inf}^2}$ at $x^* = 3.0304$,, on the $z^* = 0$ plane.

In Figure 4 the averaged Reynolds stresses in the streamwise, and spanwise, directions are presented. One can immediately notice the same pattern in all these

profiles, two peaks at approximately $y^* = 0.4 - 0.5$ and a small conical depression with big oscillations in value between them, that gets sharper as we move along x^* in the wake, which is verified for all cases. Across all fluctuation profiles it is noticeable that for each mesh, the DES methods present higher Reynolds stresses values and closer to the PIV ones, meaning that the DES method is resolving more of the turbulence than PANS, inside the the wake. The PIV values are in all cases, always significantly larger than the ones obtained in the numerical simulations, and the PIV results present fluctuation values at the tips of the profiles with values significantly larger than zero, which doesn't happen with the numerical simulations.

1) Flow visualization: In this section a description of the flow is presented, together with the comparison between the visualizations of the flow features of the PANS and DES methods using a coarse, medium and fine mesh. This includes the comparison between the visualization of time-averaged velocity and streamlines obtained, and comparison of the critical points present and its locations.

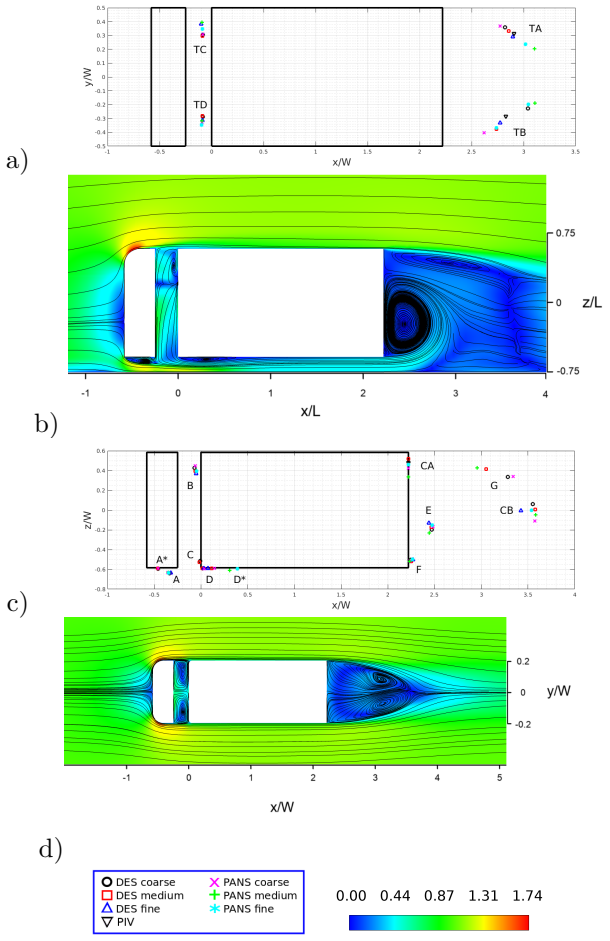

Figure 5: Localization of critical points in the plane: a) $z = 0$, c) $y = 0$ for the different cases. Contours of normalized time-averaged velocity and streamlines results using the medium mesh with PANS.

The following paragraphs will consist on the analysis and comparison of the flow structures and behaviour represented in Fig. 5.b), d), complemented with the vortex core and critical points location represented in Fig. 5.a), c). Along all methods and meshes used, the resulting flow topology was the same, with only some differences on the location of the critical points, which can be seen in Fig. 5.a), c).

First, the analysis of the results on the plane $y = 0$ will be carried out: As the flow behaviour is easy to explain outside the gap and wake region, the explanation for that region will be skipped. As the flow contours the cabin, part of it travels into the gap between the cabin and the trailer. Here the flow is fairly similar between PANS and DES, along the three meshes, as all results present a bifurcation of the flow across the gap, which is caused by the dominating flow coming from the sides of the cabin in that region, with a rotating vortex above it, vortex B, and a downwards flow stream below, also dominated by the mass flow from the sides. One noticeable difference between cases is that all PANS results present a significantly bigger recirculation bubble underneath the trailer, identified as vortex D on Fig. 5.c), when compared to the DES results. Moving on to the wake of the trailer, we find the major contributor of the truck's drag, the trailer wake vortices. Again, the flow on the wake region is structurally equivalent on the plane $y = 0$, across the methods and meshes. The wake is constituted by two main vortices rotating in opposite directions, vortex E and G. The flow traveling on top of the trailer is always attached and it contours the recirculation zone on the wake of the trailer in a slightly downward direction, without piercing it. The flow coming from underneath the trailer is mostly fed into the main lower vortex, vortex E, and there is a reversed ground boundary layer flow from around $x^* = 2.8$ to 3.7. Trapped by the main lower vortex and the feeding flow from the under-body, there is a very small secondary lower vortex, F, which is created when the flow travelling downward along the trailer's base separates, after encountering an adverse pressure gradient once it gets past vortex E. We can also see there is a saddle point and a rear stagnation point where the upper vortex, G, and the main lower vortex, E, meet, in the rear of the trailer, represented in Fig. 5.c) as CA. Also, common to all results is the presence of a node source point, identified as CB, in Fig. 5.c) - which means that the wake closure mechanism in this region is mainly caused by the flow coming from the sides of the trailer. It also means that the flow downstream of this area and some of the reversed ground boundary layer flow are also originated by the flow from the sides of the trailer. Near the main upper vortex, G, there is a free saddle point, that divides the flow in four parts: flow passing between the two main vortices, flow on the main upper vortex, G, flow passing above the main upper vortex and flow coming from the source point.

Next, the analysis of the results on the plane $z = 0$,

referring to Fig. 5a), d), will be carried out. Looking at the results, one can see that both methods give a fairly similar flow description on the plane $z = 0$: The flow accelerates around the A-pillars of the cabin, always remaining fully attached, and separates at the trailing edge of the cabin body, forming two symmetric counter-rotating vortices trapped inside the gap between the tractor and the trailer, denominated TC and TD, which dominate this region. The flow visualization on the plane $y = 0$ together with the one at $z = 0$, describe an half toroidal vortex in the gap and all the results show a fairly symmetric flow in the gap, as it can be seen in 5.a). As the flow reaches the trailer side walls, it remains attached to them along the entire length. As the PIV experiments carried out were focused on the plane $z = 0$ at the wake, a close-up comparison of this is presented on Fig. 6, where the time-averaged streamwise component of velocity is presented, together with the streamlines.

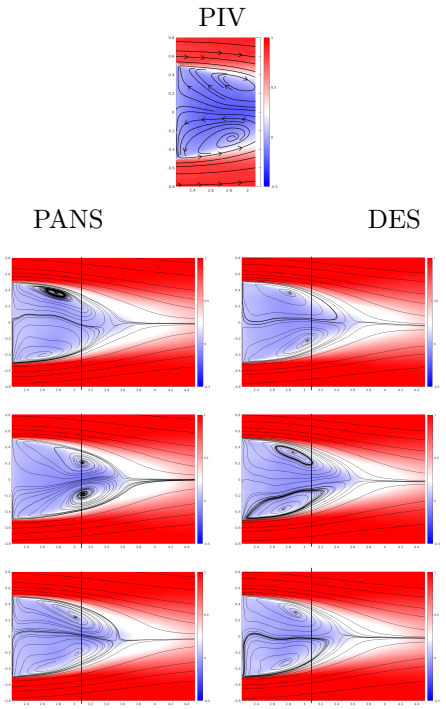

Figure 6: Contours of normalized time-averaged velocity and streamlines results from PIV and using coarse (first row), medium (second row) and fine (third row) grids with PANS and DES. The black line in the simulation results show the limit of the PIV frame

The wake of the trailer is dominated by two large vortices with opposite rotation, TA and TB, which are bounded by the mass flow from the side surfaces of the trailer, and unite into a saddle point. Due to the symmetric geometry of the model and a zero yaw angle setting, a fully symmetric flow around the truck would be expected. However, this is not what the results show. In the wake of the trailer all the results present a certain degree of asymmetry, although the PIV results presenting a fairly close to symmetric wake. This asymmetry would not exist if higher averaging times were carried out, in order for the flow to better stabilize.

V. Dynamic Results

In this section, the PANS model is used to study the effect of the application of AFC on a dynamic oscillating configuration of a truck model, which is a flow configuration that is closer to reality.

A. Drag Coefficient

The application of active flow control to the trailer's front pillar under the described oscillating conditions aims to smooth and stabilize the flow around the trailer and to minimize the hysteresis effect, ultimately leading to an overall drag reduction on the truck model.

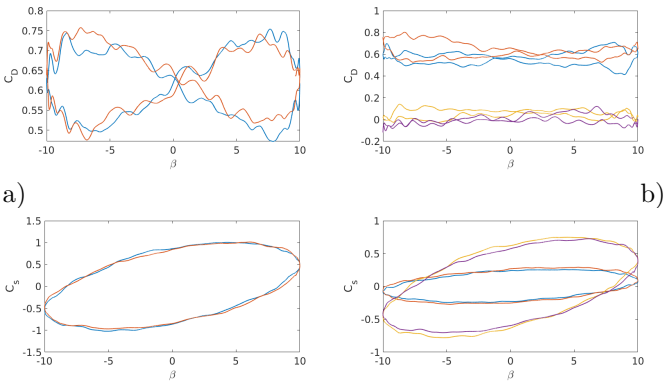

Figure 7: C_d of the complete truck, a), and cabin and trailer components, b), and C_s of the complete truck, c), and cabin and trailer components, d).
a) and c): Orange - AFC on, Blue - AFC off
b) and d): Blue - Cabin with AFC off, Orange - Cabin with AFC on, Yellow - Trailer with AFC off, Purple - Trailer with AFC on

However, by looking at Fig. 7, a), one can see that the application of AFC on the trailer's front pillars actually is not an effective solution, as Fig. 7.a), shows that the application of AFC leads to an increase of the truck's drag coefficient along almost all the yaw angles and no improvement of the hysteresis effect is seen. Over a full oscillation, the average C_d of the truck has increased 2%, which renders its use as ineffective in drag reduction, at least at this actuation frequency and configuration. Also, from Fig. 7.c), one can see that the application of AFC barely had any effect on the side force coefficient, C_s, failing to decrease the hysteresis effect.

To better understand why the AFC application is ineffective, it is important to look at both bodies of the truck model, the cabin and the trailer. The figure 7.b) shows the different drag signals of the cabin and trailer on the

dynamic actuated and unactuated cases, and it is possible to verify that the application of AFC caused an increase of the cabin's average C_d of 12.3% over a full oscillation, while the trailer's C_d had a reduction of the average C_d of 127.5%. However, the cabin is the major contributor for the full truck drag coefficient, showing values one order of magnitude higher for some yaw angles, which makes the trailer reduction of C_d being 15.3% lower than the cabin C_d increase.

B. PANS performance

During the simulation of both cases, an interesting behaviour of the PANS blending function, f_k, was noticed. Figure 8 shows the input f_k ratio of both cases, and one can see that the model is treating most of the flow with a close to DNS approach, meaning that the model is ineffective with the dynamic settings used in this simulations, more precisely, the application of unsteady inflow conditions of this magnitude, as it imposes some turbulent content that is enough to trigger the PANS model into activating the DNS mode, even though the mesh is not fine enough. This should be taken into consideration when reading this section. However, It is important to notice that the small structures that are present in the shear layer, formed on the the trailer front pillars, are still being captured, which is of great importance due to their dynamically importance for the side wake formation. This has given a further inside into a new formulation of PANS, which will have an improved f_k function, that distinguishes the turbulent fluctuations.

A solution to this problem is imposing the model rotation by mesh deformation on a circular portion of the mesh, around the model, as successfully applied in [6]. It would also be interesting to see if the IDDES model used on the static cases would perform better with the simulation settings here presented, as the IDDES is equipped with a WMLES branch which is activated for unsteady inflow conditions.

Figure 8: Contours of the f_k ratio of the dynamic simulation results at $\beta = 8.8°$ (clockwise rotation), on the plane $y = 0$ for the unactuated case. Blue represents $f_k = 0$.

VI. Conclusion

Unsteady numerical simulations were carried out to understand the physics of the flow around a simplified tractor-trailer model at $\mathrm{Re} = 2.5 \times 10^5$, as well as to conduct a detailed comparison of the PANS and DES performance in predicting the unsteady turbulent flow, and its behaviour to different levels of grid refinement. The comparison of PANS and DES in predicting the flow, using three different refinement level grids, was carried out trough the analysis of the aerodynamic forces, velocity and Reynolds stress profiles and identification and localization of the flow features through the analysis of averaged streamlines.

The results show that PANS and DES predict very similar values of C_d, across all the three meshes and between methods. The same is verified for C_l for the DES results, and for the PANS results when using medium and fine mesh, while with coarse mesh the PANS results present significantly different C_l values from the other results, specially for the cabin.

In the wake, u/U_{inf} profiles obtained from the numerical simulations always over-predicts the magnitude when compared to the PIV results, while for the Reynolds stresses profiles, the opposite happens, it under-predicts. Both methods, across all meshes, don't capture the peaks of the profiles precisely, but almost all capture the trends present in PIV results. In the wake it is the DES results that present higher Reynolds stresses profiles and come closer to the PIV results.

The results show that both PANS and DES simulations capture the same main flow features and produce similar trends, which are in accordance with works such as [1, 19, 20], between others.

Overall, the DES results are more correlated, as the profiles taken along the trailer and along the wake mostly overlap, from the coarsest mesh to the finest, which is not the case for PANS as the coarse profiles are noticeably different from the ones obtained using finer meshes and even the finer meshes don't overlap as good as the DES ones.

The second part of the thesis was focused on providing a first look into how viable the application of AFC in the trailer front pillars is, in order to mitigate the flow separation and consequently enhancing its aerodynamic performance on the gap region, during close to real conditions. The dynamic simulation results showed the creation of an hysteresis effect on the C_d and C_s signals, created by the inertia of flow during the oscillations. When it comes to the effect of the actuation on the dynaimc case, it was possible to see that the flow is not stabilized by the AFC, as the hysteresis of the C_d and C_s signals were not decreased. Most important, it was observed an overall increase of C_d due to the AFC application, as the decrease in the trailer's C_d was not enough to counteract the increase of the cabin's C_d, suggesting the need to change the AFC configuration and/or parameters in order to obtain better results.

As PANS failed to effectively use its bridging capabilities to treat the dynamic flow under the applied settings, it was concluded that the use of PANS is ineffective to study dynamic cases, when the oscillation is imposed by the boundary layers, since it introduces some turbulent content that is enough to trigger the PANS model into activating the DNS mode.

VII. Future Work

Both two parts of the thesis present aspects that should be worked on. In the comparison between DES and PANS methods there is a lack of experimental results necessary to distinguish which of the methods represent the unsteady turbulent flow more accurately.

On the dynamic cases, it was concluded that the way the oscillation was introduced to the case is not supported by PANS. So, a mesh deformation on a circular portion of the mesh around the model should be applied, as successfully applied in [6].

Since the AFC application was rendered ineffective for the one configuration used, different configurations should be considered, such as setting the actuation slot in a different position of the pillar or to apply an actuation at a different angle with the surface.

References

[1] H. Choi, J. Lee, and H. Park, "Aerodynamics of Heavy Vehicles," *Annual Review of Fluid Mechanics*, vol. 46, pp. 441–468, 2014.

[2] J. Zhang, J. juan Li, H. qi Tian, G. jun Gao, and J. Sheridan, "Impact of ground and wheel boundary conditions on numerical simulation of the high-speed train aerodynamic performance," *Journal of Fluids and Structures*, vol. 61, pp. 249–261, 2016.

[3] E. Guilmineau, G. B. Deng, and J. Wackers, "Numerical simulation with a DES approach for automotive flows," *Journal of Fluids and Structures*, vol. 27, no. 5-6, pp. 807–816, 2011.

[4] S. Krajnović, R. Lárusson, and B. Basara, "Superiority of PANS compared to LES in predicting a rudimentary landing gear flow with affordable meshes," *International Journal of Heat and Fluid Flow*, vol. 37, pp. 109–122, 2012.

[5] G. Minelli, E. A. Hartono, V. Chernoray, L. Hjelm, B. Basara, and S. Krajnović, "Validation of PANS and active flow control for a generic truck cabin," *Journal of Wind Engineering and Industrial Aerodynamics*, vol. 171, pp. 148–160, 2017.

[6] G. Minelli, S. Krajnovic, and B. Basara, "A Flow Control Study of a Simplified, Oscillating Truck Cabin Using PANS," *Journal of Fluids Engineering*, vol. 140, no. 12, p. 121101, 2018.

[7] M. El-Alti, V. Chernoray, M. Jahanmiri, and L. Davidson, "Experimental and Computational Studies of Active Flow Control on a Model Truck-trailer," *EPJ Web of Conferences*, vol. 25, no. 16, 2012.

[8] B. Chiekh, M. Ferchichi, M. Michard, M. Guellouz, and M. S. Béra, "Synthetic Jet Actuation Strategies for Momentumless Trailing Edge Wake," *Journal of Wind Engineering and Industrial Aerodynamics*, vol. 113, pp. 59–70, 2013.

[9] C. Håkansson and M. J. Lenngren, "CFD Analysis of Aerodynamic Trailer Devices for Drag Reduction of Heavy Duty Trucks," *Chalmers tekniska högskola*, 2010.

[10] S. K. Arolla and P. A. Durbin, "Modeling rotation and curvature effects within scalar eddy viscosity model framework," *International Journal of Heat and Fluid Flow*, vol. 39, pp. 78–89, 2013.

[11] F. Menter, "Zonal Two Equation k-w Turbulence Models For Aerodynamic Flows," in *23rd Fluid Dynamics, Plasmadynamics, and Lasers Conference*, 1993.

[12] F. R. Menter, "Two-equation eddy-viscosity turbulence models for engineering applications," *AIAA Journal*, vol. 32, no. 8, pp. 1598–1605, 1994.

[13] M. L. Shur, P. R. Spalart, M. K. Strelets, and A. K. Travin, "A hybrid RANS-LES approach with delayed-DES and wall-modelled LES capabilities," *International Journal of Heat and Fluid Flow*, vol. 29, no. 6, pp. 1638–1649, 2008.

[14] S. Watkins and J. Saunders, "Turbulence Experienced by Road Vehicles under Normal Driving Conditions," *SAE Technical Paper Series*, vol. Paper 9509, 1995.

[15] S. Wordley and J. Saunders, "On-road Turbulence," *SAE Int. J. Passeng. Cars - Mech. Syst*, 2009.

[16] ——, "On-road Turbulence: Vol. 2," *SAE International Journal of Passenger Cars - Mechanical Systems*, vol. 2, pp. 111–137, 2009.

[17] A. Harten, "High resolution schemes for hyperbolic conservation laws," *Journal of Computational Physics*, vol. 49, no. 3, pp. 357–393, 1983.

[18] P. H. Gaskell and A. K. C. Lau, "Curvature-compensated convective transport: SMART, A new boundedness- preserving transport algorithm," *International Journal for Numerical Methods in Fluids*, 1988.

[19] D. McArthur, D. Burton, M. Thompson, and J. Sheridan, "On the near wake of a simplified heavy vehicle," *Journal of Fluids and Structures*, vol. 66, pp. 293–314, 2016.

[20] H. J. Schmidt, R. Woszidlo, C. N. Nayeri, and C. O. Paschereit, "The effect of flow control on the wake dynamics of a rectangular bluff body in ground proximity," *Experiments in Fluids*, vol. 59, no. 6, p. 0, 2018.